Optics & Laser Technology 176 (2024) 111022

Contents lists available at ScienceDirect

Optics and Laser Technology

journal homepage: www.elsevier.com/locate/optlastec

Full length article

Development of a selective wet-chemical etchant for precise 3D sculpting of silicon enabled by infrared non-linear laser modification

Mona Zolfaghari Borra [a,b,1], Behrad Radfar [a,b,c], Hisham Nasser [a], Tahir Çolakoğlu [a,d], Onur Tokel [e,f], Ahmet Turnalı [g,h], Merve Demirtaş [i,j], Dilek Işık Taşgın [k], Hande Üstünel [b,l], Daniele Toffoli [l,m], Fatih Ömer İlday [e,g,2], Raşit Turan [a,b,i], Ihor Pavlov [a,b,i], Alpan Bek [a,b,i,*]

[a] ODTÜ-GÜNAM, Middle East Technical University (METU), 06800 Ankara, Turkey
[b] Micro and Nanotechnology Graduate Program of Natural and Applied Sciences, Middle East Technical University (METU), 06800 Ankara, Turkey
[c] Department of Electronics and Nanoengineering, Aalto University, Tietotie 3, FI-02150 Espoo, Finland
[d] Department of Physics Engineering, Ankara University, 06100 Ankara, Turkey
[e] Department of Physics, Bilkent University, 06800 Ankara, Turkey
[f] UNAM National Nanotechnology Research Center and Institute of Materials Science and Nanotechnology, Bilkent University, Ankara 06800, Turkey
[g] Department of Electrical and Electronics Engineering, Bilkent University, 06800 Ankara, Turkey
[h] Department of Electrical and Computer Engineering, Boston University, 8 Saint Mary's Street, Boston, MA 02215, USA
[i] Department of Physics, Middle East Technical University (METU), 06800 Ankara, Turkey
[j] Network Technologies Department, TUBITAK ULAKBIM, 06800 Ankara, Turkey
[k] Department of Inter-Curricular Courses, Çankaya University, 06790 Etimesgut, Ankara, Turkey
[l] Department of Chemical and Pharmaceutical Sciences, Trieste University, Trieste, Italy
[m] IOM-CNR, Istituto Officina dei Materiali, 34149 Trieste, Italy

ARTICLE INFO

Keywords:
Laser treatment
Silicon
Wet etching
Amorphous materials
Analytical methods

ABSTRACT

Recently-demonstrated high-quality three-dimensional (3D) subsurface laser processing inside crystalline silicon (c-Si) wafers opens a door to a wide range of novel applications in multidisciplinary research areas. Using this technique, novel maskless micro-pillars with precise control on the surface reflection and coverage are successfully fabricated by etching the laser-processed region of the c-Si wafer. To achieve this, a particular selective wet chemical etching is developed to follow subsurface laser processing of c-Si to reveal the desired 3D structures with smooth surfaces. Here, we report the development of a novel chromium-free chemical etching recipe based on copper nitrate, which yields substantially smooth surfaces at a high etch rate and selectivity on the both laser-processed Si surface and subsurface, i.e., without significant etching of the unmodified Si. Our results show that the etch rate and surface morphology are interrelated and strongly influenced by the composition of the adopted etching solution. After an extensive compositional study performed at room temperature, we identify an etchant with a selectivity of over 1600 times for laser-modified Si with respect to unmodified Si. We also support our findings using density functional theory calculations of HF and Cu adsorption energies, indicating significant diversity on the c-Si and laser-modified surfaces.

1. Introduction

Recently, we have succeeded in 3D microstructuring of Si via direct laser-writing deep inside its bulk through a method that relies on a self-organized mechanism [1,2] while the efforts dating until 2005 [3] were largely unsuccessful. Our method is an adaptation of another self-organized technique, known as nonlinear laser lithography that we developed to create self-organized sub-wavelength structures on

* Corresponding author at: Department of Physics, Middle East Technical University (METU), 06800 Ankara, Turkey.
E-mail addresses: mborra@metu.edu.tr (M. Zolfaghari Borra), behrad.radfar@aalto.fi (B. Radfar), nasser@metu.edu.tr (H. Nasser), tcolakoglu@ankara.edu.tr (T. Çolakoğlu), otokel@bilkent.edu.tr (O. Tokel), turnali@bu.edu (A. Turnalı), merve.demirtas@tubitak.gov.tr (M. Demirtaş), ditasgin@cankaya.edu.tr (D. Işık Taşgın), ustunel@metu.edu.tr (H. Üstünel), toffoli@units.it (D. Toffoli), ilday@bilkent.edu.tr (F.Ö. İlday), turanr@metu.edu.tr (R. Turan), ipavlov@metu.edu.tr (I. Pavlov), bek@metu.edu.tr (A. Bek).
[1] Currently at Nanotam, Bilkent University (email: m.zolfagharibora@gmail.com).
[2] Currently at Ruhr University Bochum (email: oemer.ilday@ruhr-uni-bochum.de).

https://doi.org/10.1016/j.optlastec.2024.111022
Received 16 October 2023; Received in revised form 14 March 2024; Accepted 10 April 2024
Available online 17 April 2024

surfaces [4]. In both 2D and 3D implementations of nonlinear laser lithography, we exploit an intrinsic feedback mechanism, where the pulses cause changes in the material that alter how the subsequent pulses focus. In the case of 3D Si modification, these changes constitute rod-like elongated structures along the beam propagation direction. The length of the rods can be changed by the laser parameters and the number of incident pulses. They can also be positioned at an arbitrary depth below the surface where the laser modification results in a change of the material's optical index. Thus, we have demonstrated a variety of structures of interest for various applications, including optical waveguides, information storage, holographic structures, and Fresnel lenses for the near-IR, among others. We have further shown that the laser-modified regions of Si can be selectively etched to reveal various 3D structures [1]. Today, laser-processing of Si is an active area where a wide variety of applications have been demonstrated and reviewed in [5], including quantum photonics [6], lab-on-chip [7–10], optical communications [11], and microfluidics [12–14]. An emerging application demonstrated by this technique is laser-assisted Si slicing (LASIS) [1], in which the fabricated thin c-Si slices can be processed into thin/ultra-thin Si solar cells produced with a minimum loss of Si material [15,16]. Low material loss in slicing is an important requirement in reducing the solar cell cost. However, the vast majority of the studies on laser-based 3D processing of Si are limited to the creation of optical index variations with few demonstrations of the chemical etching to create standalone 3D structures. For revealing the 3D laser-sculpted structures out of Si bulk, laser-modified regions of the c-Si subsurface are removed by selective chemical etching. We attribute the slow development of this area to the lack of a well-developed etchant, which we address here. In contrast to 3D or volume laser processing, surface laser processing is a well-established technique to create desired features on the Si surface. For instance, laser-induced periodic surface structuring (LIPSS) is used to create light-trapping interfaces for solar cells [17–21] or fabrication black-Si [22–24].

In laser-assisted processing of Si, ultra-short near to mid-infrared laser pulses are focused into the bulk of the wafer. The interaction of the intense localized laser radiation with Si induces non-linear effects such as multi-photon absorption, self-focusing, and plasma generation inside the focal volume [25–27]. The subsurface laser processing provides precise local modifications at the targeted sites regardless of Si crystallinity or orientation [28,29]. In this technique, the optimization of the laser parameters (i.e., laser wavelength, pulse duration, and pulse energy) enables precise control over the laser-Si interaction. The formation of subsurface structures using a nanosecond or femtosecond pulsed laser beam [30–34] is a new micro and nanofabrication approach [35,36] for various applications which require high-quality structures. This method creates modification at localized regions with minor damage on the c-Si surface [1,2].

So far, neither the surface nor subsurface laser processing of Si has yet been investigated enough to unearth the full potential of 3D laser processing for the microfabrication of Si devices. We lack a well-established method to remove the laser-modified regions without damaging unprocessed areas. A natural outcome of surface laser processing is the intentional damage it induces to some surface areas. Therefore, a specially tailored selective etchant must be developed to remove only the laser-damaged regions. Researchers have invested substantial efforts in Si technology to control the defect densities associated with re-growth and Si wafer processing [37]. Selective chemical etching is a simple route to reveal the number of defects in c-Si. Chemical treatments typically comprise a redox reaction to etch the defects selectively. In a more general view, it is of great essence that such a special etchant is developed to selectively remove laser-modified Si out of the c-Si wafer to sculpt functional 3D structures.

Etching is an essential step in the micro- and nanofabrication of c-Si-based devices. Among different etching techniques, solution-based chemical etching offers a low-cost and facile alternative compared to conventional plasma-enhanced gas-phase etching counterparts while yielding a high surface and bulk material quality due to the absence of plasma damage. Achieving a Si surface as defect-free as possible at microscale is crucial to ensure high performance of Si devices, such as micro-electromechanical systems (MEMS) [38–41], micro-optics [42–44], photonic devices, integrated circuits, and photovoltaic solar cells [21,45–51].

Similar to surface laser processing, a subsequent chemical etch is needed to reveal the subsurface structures without altering unprocessed Si regions for the aforementioned wide applications. To this end, we need an etchant with excellent selectivity (the ratio of the removal rate of laser processed and pristine regions) and a high etch rate. Thus far, typical defect etchant recipes comprise nitric acid (HNO_3) or chromium (Cr)-based chemical solutions, which both serve as the oxidizing agent of Si surface. The HNO_3-based etchants, including HNA [52] and Dash etch (1956) [53] are crystallographic orientation and dopant type independent; however, they require highly doped Si (HNA) or high-temperature and longer process duration (Dash). Other etchants use a Cr-based oxidizing agent to delineate defects and dislocations in Si, including the Sirtl etch (1961) [54] and Seiter etch (1977) [55]. While the Sirtl etch works well only for $\langle 1\,1\,1\rangle$ oriented surfaces, the Seiter etch works well on $\langle 1\,0\,0\rangle$.

A highly selective etching solution of Si defects in the advanced electronics industry is the MEMC etching (Monsanto Electronic Materials Company – 1987) [56] which is a copper nitrate – $Cu(NO_3)_2$-based etchant and applies to both p- and n-doped Si. MEMC etch has a long lifetime during room-temperature processes and generates undesired pits on both $\langle 1\,1\,1\rangle$ and $\langle 1\,0\,0\rangle$ oriented surfaces. Its planar etch rate is the same for all crystallographic directions, while the etching uniformity is similar to that of Sirtl. Moreover, as it is a Cr-free solvent, it is relatively environmentally friendly compared to Cr-based etchants. It is commonly used in the destructive characterization of Si-wafer quality in industrial applications. In MEMC etch, the HNO_3 oxidizing agent oxidizes the Si surface, and hydrofluoric acid (HF) dissolves the formed SiO_2 while adding $Cu(NO_3)_2$, in particular, assists in reducing the resultant point defects. Therefore, the amount of $Cu(NO_3)_2$ in the mixture dramatically influences the localized differential oxidation at the defect sites. Although a detailed explanation of the mechanism is unknown, it is commonly accepted that CH_3COOH of MEMC acts as a moderation agent of the surface reaction through limiting the oxidation. When the etchant solution contains too much CH_3COOH, the concentration of the oxidizing agent decreases, resulting in the impairment of the oxidization. This precludes a high etch rate. If the amount of CH_3COOH is too small, the etching becomes too fast, increasing the surface roughness [57].

We adopted the MEMC etch to develop an optimized etchant for 3D nonlinear infrared laser-assisted sculpting of Si. This solution is highly defect-sensitive, which increases its selectivity in favor of the laser-modified regions. The solution depends on the crystal orientation and the dopant type. The etch durations are reasonably short. The solution has a long lifetime, making refreshing the chemical concentration (known as spiking) unnecessary. In addition, Cu is cheaper, relatively less toxic, and more environmentally friendly owing to being Cr-free [58]. In contrast, the Sirtl and Seiter etches yield toxic, even carcinogenic reaction byproducts [59]. Their use is heavily regulated in many countries.

This work focuses on the development of a chemical solution for selective etching of the laser-modified surface and subsurface Si regions at high etch rates. We first present the ultimate potential of the proposed development in 3D sculpting using our champion etchant. Our champion etchant is an optimized etching recipe which meets the requirements of a reasonable etch rate and smooth Si facets. We support our findings via density functional theory (DFT) calculations that provide an atomistic-level understanding on how the etchant components interact with the surfaces in question.

2. Perspectives on 3D sculpting

Micro-pillar arrays have been of interest for solar applications due to the increased light trapping and high carrier collecting efficiency inherent in the pillar structure [60]. Light trapping of the incoming solar light can be achieved by texturing the front surface of the solar cell. Numerous methods are available, including nanowires [61], inverted pyramids [62], plasmonic metal NPs [47], etc. As an application of 3D sculpting, we demonstrate the laser-based fabrication of micron-size pillars array on c-Si wafers. Micro-pillar arrays on the surface of Si wafers can be used in solar cell design in which light can be effectively trapped via multiple reflections between pillars. Another application can be the fabrication of MEMS resonators for various applications requiring mechanical modulation [63,64]. This technology allows obtaining a controllable size/depth combination of the pillar in the various ranges in two-step fabrication in Si substrate. Fig. 1 depicts the fabrication procedure of micro-pillar arrays. The first step is laser processing which induces structural modification of Si which results in amorphous/poly phase silicon (details in Supporting Information 5). Inverse pillar structures are directly written by a raster scan of the focal spot on and in the Si wafer (Fig. 1 (a)). The laser processing parameters are presented in section 3.1. Laser-Induced Si Modification. Next, in the second step, the laser-processed regions are removed by our *champion* selective etchant to extract the Si micro-pillar structure (Fig. 1 (b)). For solar cell applications, the light trapping characteristics of the micro-pillar array can be investigated against varying depths and sizes of micro-pillar arrays (Fig. 2). With this technique, micro-pillars with an area as small as $\sim 9 \times 9\ \mu m^2$ and with a depth as large as 118 μm were successfully fabricated yielding an impressive aspect ratio > 13.

Fig. 2 shows micro-pillar arrays of 9 μm × 9 μm, 32 μm × 32 μm, and 57 μm × 57 μm pillar area. In Fig. 2(b), (d), and (f) a light blue and a light brown box mark the pillar and the spatial period, respectively. Considering ratio of the blue/brwn marked box areas, surface coverages of ~ 5 %, ~25 %, and ~ 56 % are achieved for 9 μm × 9 μm, 32 μm × 32 μm, and 57 μm × 57 μm pillar areas in Fig. 2(b), (d), and (f), respectively. A total area of 2 mm × 2 mm micro-pillar arrays each are revealed in 20 min of the etch duration for all sizes.

As a simple demonstration of the application potential of direct laser-written 3D microstructuring of Si, we show how such high-aspect micropillar arrays can be utilized in efficient light trapping. Fig. 3 shows that the 32 μm x 32 μm micro-pillar array resulted in the lowest reflectance among micro-pillar arrays (meaning an absolute 25 % light trapping on average over entire spectral range), all of which exhibited significant light trapping activity as compared to the unstructured surface.

3. Methods

In this study, the samples were prepared from double-side polished, single-crystalline boron-doped p-type Si wafers with ⟨1 0 0⟩ orientation (Siegert Wafer). Two different sets of samples were prepared for the laser processing: (i) For subsurface modifications, the Si wafers had a thickness of 525 μm and a resistivity of 1–5 Ω.cm. (ii) For surface modifications, Si wafers with a thickness of 1000 μm and resistivity of 1–10 Ω.cm were used. With these two methods of preparation, we aimed to demonstrate an etching profile for both Cross-sectional Accessible Laser Processed (CALP) and Surface Accessible Laser Processed (SALP), which are discussed below. After the laser processing, the samples were treated with various etch recipes while systematically varying the components adopted from MEMC to determine the optimal composition.

3.1. Laser-induced Si modification

All Si modifications were done by 3D subsurface laser processing; however, the extent of subsurface modifications toward the surface was different for different samples. The laser system was an in-house built nanosecond fiber laser, producing up to 5 W of average power at a wavelength of 1550 nm. The repetition rate of the laser was adjustable

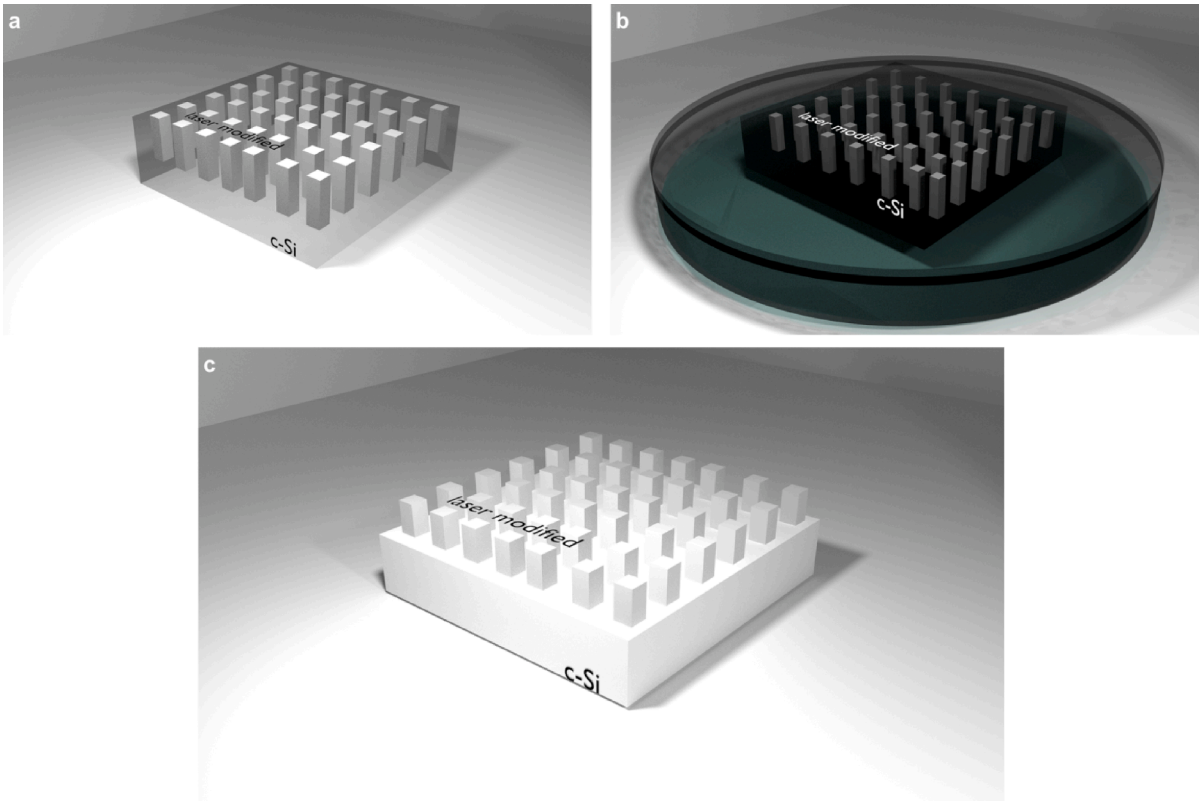

Fig. 1. Steps of micro-pillar fabrication: (a) Modified part after patterning the pillars via laser processing; (b) Selective chemical etching; (c) Pillar arrays.

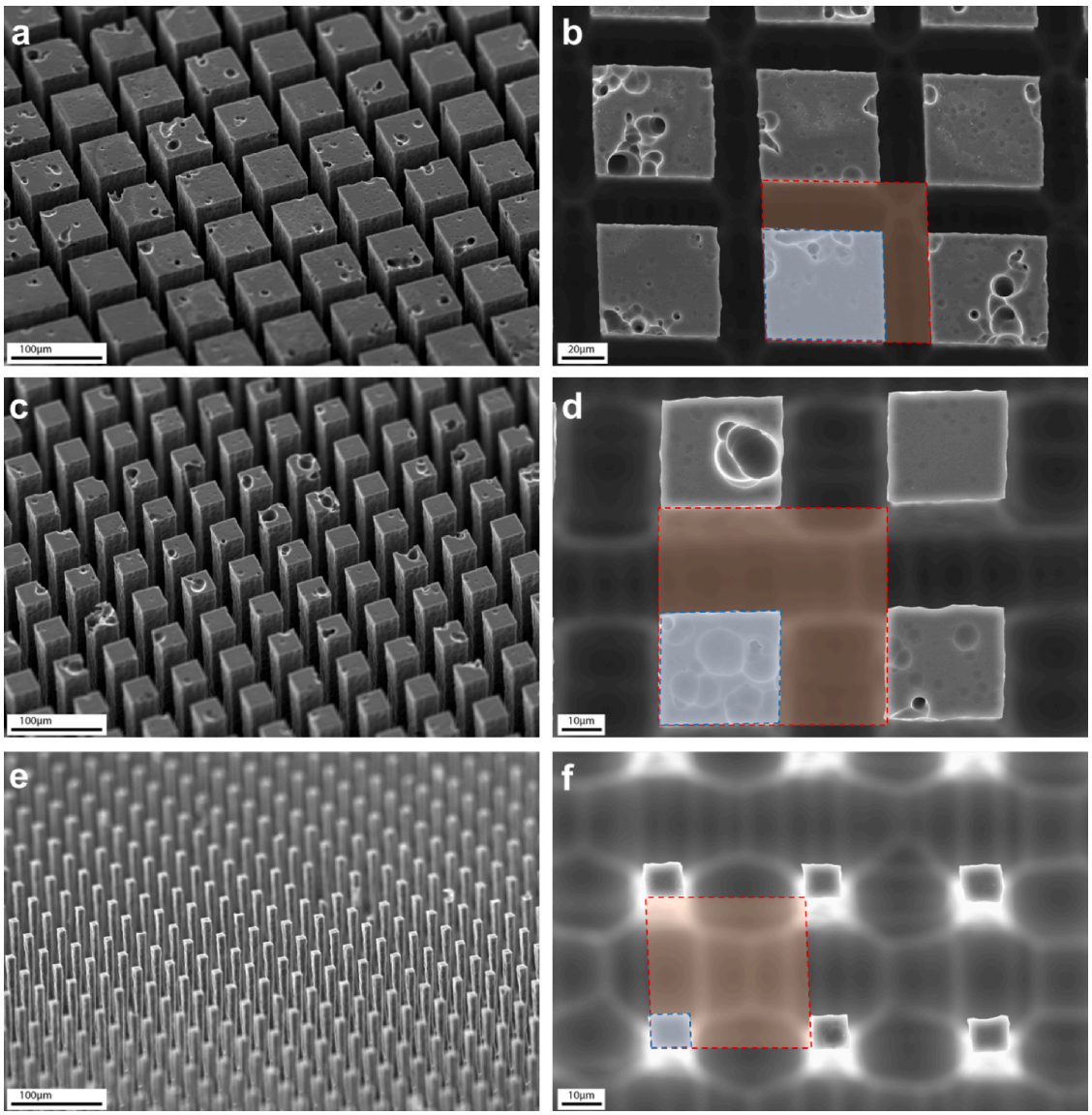

Fig. 2. SEM images of micro-pillar arrays (a, c, e) 40° tilt; Micro-pillar (b, d, f) top surface sizes: (a, b) 57 µm × 57 µm, (c, d) 32 µm × 32 µm, (e, f) 9 µm × 9 µm, and pulse energy 3 µJ.

between 100 kHz to 1 MHz, limited by the generation of amplified spontaneous emission (ASE) at a low repetition rate. In the experiments, the repetition rate of the laser was 100 kHz having a maximum pulse energy of 50 µJ and a pulse duration of ~ 5 ns. While we observed that pulse energies higher than 2.5 µJ make the modifications that could be etched, pulse energies lower than 2.5 µJ did not make sufficiently selective etched modifications. Therefore, we continued to use pulse energies of 2.5 µJ and higher in our experiments. For the specific presented application, i.e. micro-pillars, we used a pulse energy of 3 µJ to achieve high aspect ratio in depth. The laser beam was focused inside the samples by an aspheric lens (NA = 0.3, f = 8 mm). The polarization direction was along the vertical direction with respect to the optical table during these experiments when the laser beam was parallel to the optical table. We note that we did not observe any effect of polarization direction with respect to Si crystal orientation on the properties of the processed region. The samples with dimensions of 10 mm × 10 mm were mounted on a 3D motorized translation stage for scanning in all directions with sub-micron resolution.

Two different sets of samples were prepared for different opening access to the laser-modified region. For the first type, the laser was focused into the sample from the cross-sectional direction, and the sample was raster scanned laterally (in the *x*-*y* direction), as shown in Fig. 4 (a). This scanning pattern forms a laser-modified plane parallel to the top surface inside the sample. The laser-modified thickness of each plane is ~ 4 µm, as confirmed by the IR camera images (Supporting video 1 – more details in Ref. [28]). Several planes were created on top of each other, forming a laser-processed zone with a thickness of ~ 30 µm, as shown in Fig. 4 (b). For this set of samples, the laser-modified zone is accessible to the etchant solutions from the cross-sectional surface at three sides with 30-µm height openings with wafer dicing (Supporting Information 1). We will call this type of sample as CALP.

For the second type of the samples, the laser beam was focused inside the sample from the top surface, and raster scanned in the *x*-*y* direction, as shown in Fig. 4 (c). The cross-sectional thickness of one plane in the *z*-*direction* is ~ 80 µm. After the creation of each plane, the samples were shifted 20 µm down in the *z*-direction (corresponding to ~ 60 µm beam shift-up of the focal point inside of the samples due to the refractive index of Si), and the next modified plane was formed with ~ 20 µm overlap with the previous one. We repeated these steps until the last laser-modified plane was created on the top surface of the samples for a total depth of ~ 450 µm, as shown in Fig. 4 (d). For this set of samples, the laser-modified zone is accessible to the etchant from the top surface

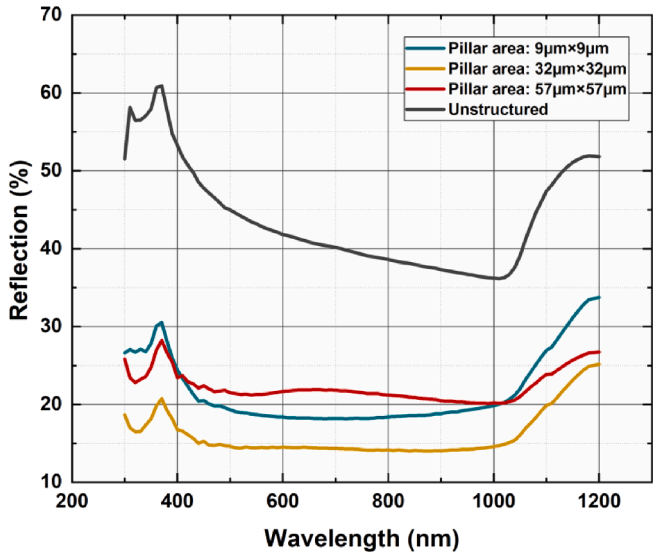

Fig. 3. Total reflectance of the fabricated Si micro-pillars with different areas and depths.

(10 mm × 10 mm area). We will refer to these as SALP samples.

3.2. Chemical etching

The effects of different etch solution mixtures are investigated on both CALP and SALP samples. Our motivation is to study the selective etching of Si in CALP configuration since it represents a universal scenario in the 3D laser structuring of Si. This process does not necessarily create large laser-processed surface areas where the etchant can quickly attack. It is essential to check the feasibility of the fabrication of 3D structures embedded inside the Si while heat transfer and diffusion constraints associated with narrow surface openings are present. As a complementary configuration, we introduced SALP structuring to create features from the surface up to the desired depth inside Si.

For the CALP structuring, the samples were diced into smaller individual samples with an area of 7.30 mm × 2.34 mm after laser modification. The dicing exposes three surfaces of the laser-modified region (one with 2.34 mm × 0.03 mm and two with 6.55 mm × 0.03 mm) to the etchant solution (see Fig. 5 (a) and Fig. S1). For the SALP structuring, the samples were diced with dimensions of 10 mm × 10 mm. The laser-modified region (2 mm × 2 mm) is exposed to the etchant from one side, vertically from the top surface (see Fig. 5 (b)). Also, a set of unprocessed Si wafers were diced with identical sizes (reference samples). Before chemical treatments, all samples were subjected to standard cleaning 1 and 2, which are used to remove organic contaminants as well as metallic and ionic contaminants from the surface of the samples, respectively [65].

As mentioned in the Introduction, MEMC solution is already used in the electronics industry for defect density determination of Si wafers. However, the MEMC solution offers a high etch rate at the expense of high selectivity and smooth surface morphology. In order to lend MEMC the preferred qualities in selectivity and surface morphology, we made a systematic analysis of the effect of each redox component [66,67] on the etching chemistry. In order to investigate the effects of HNO_3 as an oxidant, copper (II) nitrate hydrate salt ($Cu(NO_3)_2{\cdot}3H_2O$) as a catalyst [56,68], and HF as an oxide dissolvent on selectivity, etch rate, and surface morphology, the concentration of each component was varied systematically. More details regarding the redox chemical reactions and catalytic activities can be found in Supporting Information 2. In this study, 12 different sets of solutions were considered. The concentrations of the components are separated into three subgroups which are highlighted in Table 1. Within each subset, we varied only one component of the mixture. The deionized wafer (DI H_2O) is also varied to keep the solution volume fixed to 100 ml.

In addition to analyzing the effect of the above-mentioned components of the MEMC solution, we analyzed several alternative etching solutions to compare them with our etchant properties, including etch rate and selectivity. These results are presented in Supporting Information 3.

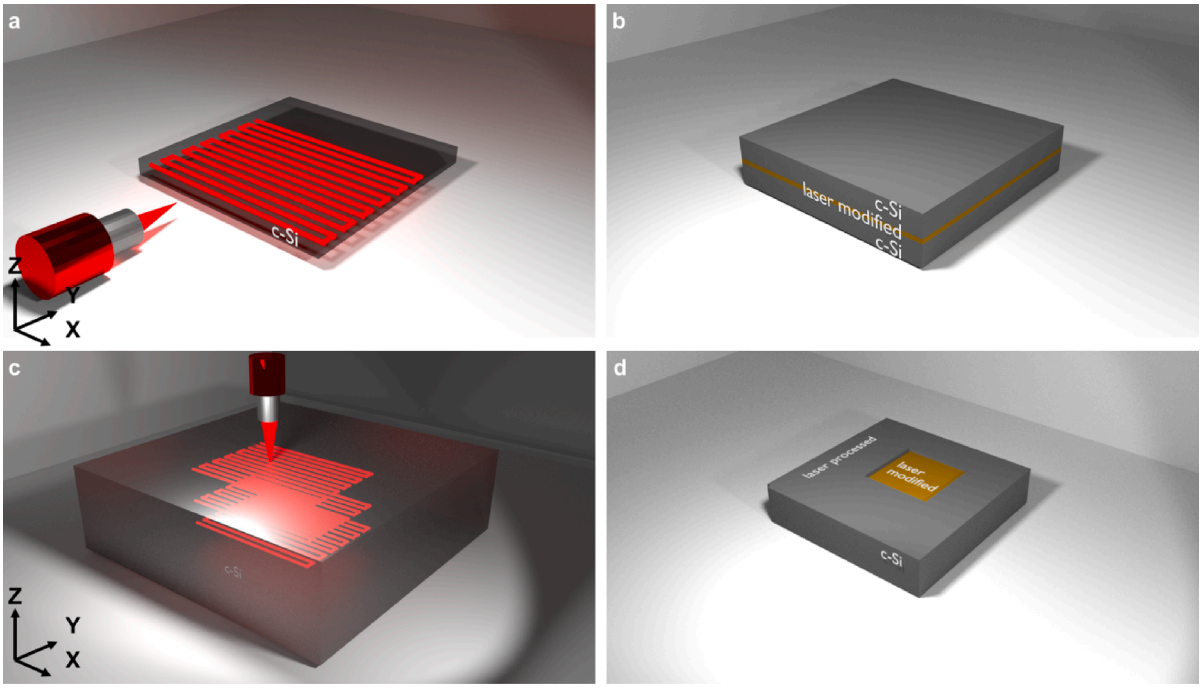

Fig. 4. (a, c) – Depiction of the laser-beam scanning direction (a) inside of c-Si for CALP samples, and (c) on SALP samples; (b, d) – 3D schematic representation of the laser processed zones for (b) CALP, and (d) for SALP.

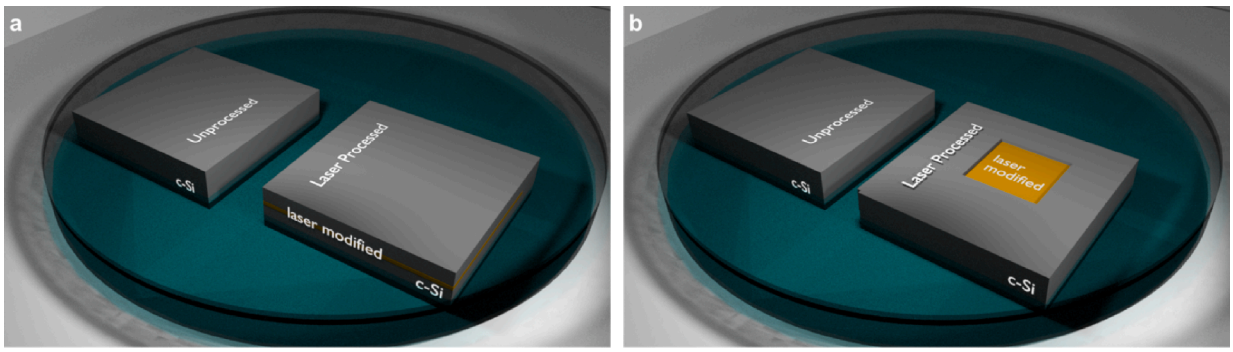

Fig. 5. Schematic representations of (a) CALP and (b) SALP samples in the chemical bath. In both cases, an unprocessed Si was added.

Table 1
Chemical composition of the solutions with different $Cu(NO_3)_2$, HF, and HNO_3 concentrations. The amount of DI H_2O is adjusted to maintain 100 ml of solution corresponding to 100 %.

	$Cu(NO_3)_2$	HF	HNO_3	CH_3COOH
	(g)	(vol%)	(vol%)	(vol%)
$Cu(NO_3)_2$Comparison	0.75	14.00	16.25	18.00
	1.25			
	1.00			
	2.00			
HFComparison	1.00	7.00	16.25	18.00
		10.00		
		12.00		
		14.00		
		16.00		
		18.00		
HNO_3Comparison	1.00	14.00	9.75	18.00
			13.00	
			16.25	
			19.50	
			22.75	

3.3. Etch rate and selectivity redefined

The quantitative assessment of surface etching in 2D follows the established concepts of the etch rate and selectivity, as developed for semiconductor fabrication [69,70]. When using lasers for etching, it seems that both etch rate (percentage of etched mass from the modified region over time, i.e., Fig. 7 (a), (d), (g)) and selectivity (the ratio of etch rates of the laser-modified and unprocessed regions) need to be redefined since the process occurs in the subsurface, where etch thickness over time is not applicable. Therefore, we have redefined these parameters by using a 3D approach that necessitates using correction factors for the geometry.

In order to calculate the mass reduction due to the etching of the laser-modified regions in each chemical mixture (which is referred to as a Set), a pair of laser-processed and unprocessed c-Si samples were placed in the same solution as depicted in Fig. 5. The mass reduction of the laser-processed sample consists of two parts, that of the laser-modified region and the remaining (unprocessed) region of the same sample. We estimated the mass reduction of the unprocessed region of the laser-modified sample by measuring the mass reduction of the unprocessed sample. Then, by incorporating proper correction factors, we modeled and calculated the mass reduction of the laser-modified region (detailed in the 4. Results and Discussion section). Various practically unmeasurable parameters are involved in these calculations in the static etching procedure. Those parameters include diffusion restriction for the mass and heat transports. Hence, proper estimation of the corresponding correction factors is essential (see 4.1. Correction Factors Calculation & Etch Pit Radius Distribution Analysis section). The SEM images taken from samples at the end of each etching process step presented in Supporting Information 4 are used to track and determine the smoothness of the surface morphology by analyzing etch pit size distribution.

In order to calculate the etch rates, mass reductions of the laser processed, and the unprocessed samples were measured by weighting the samples after etching in each solution for 60 min with 10-minute intervals for CALP and 5-minute intervals for SALP. We specifically probed the interval between 10 and 60 min of etching durations since industrial applications favor short etch durations while too short durations may not be sufficient to fully etch modified regions. Based on the obtained etch rates, we calculate the selectivity of each solution set. Hence, we assess the effect of each component to determine the corresponding properties of the solution.

3.4. Density functional theory calculations

Density functional theory (DFT) calculations were performed to understand the atomistic origins of the interaction between the etchants and the surfaces. All calculations presented here were conducted using the periodic, plane-wave-based Quantum Espresso code suite [71]. The exchange–correlation interaction was treated within the Perdew-Wang

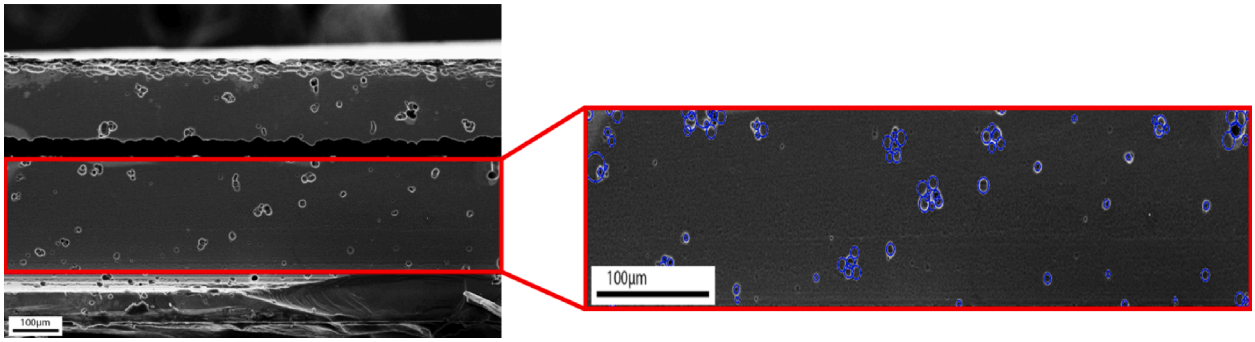

Fig. 6. The selected area for the champion etchant from cross-sectional SEM image and the result etch pit size distribution analysis.

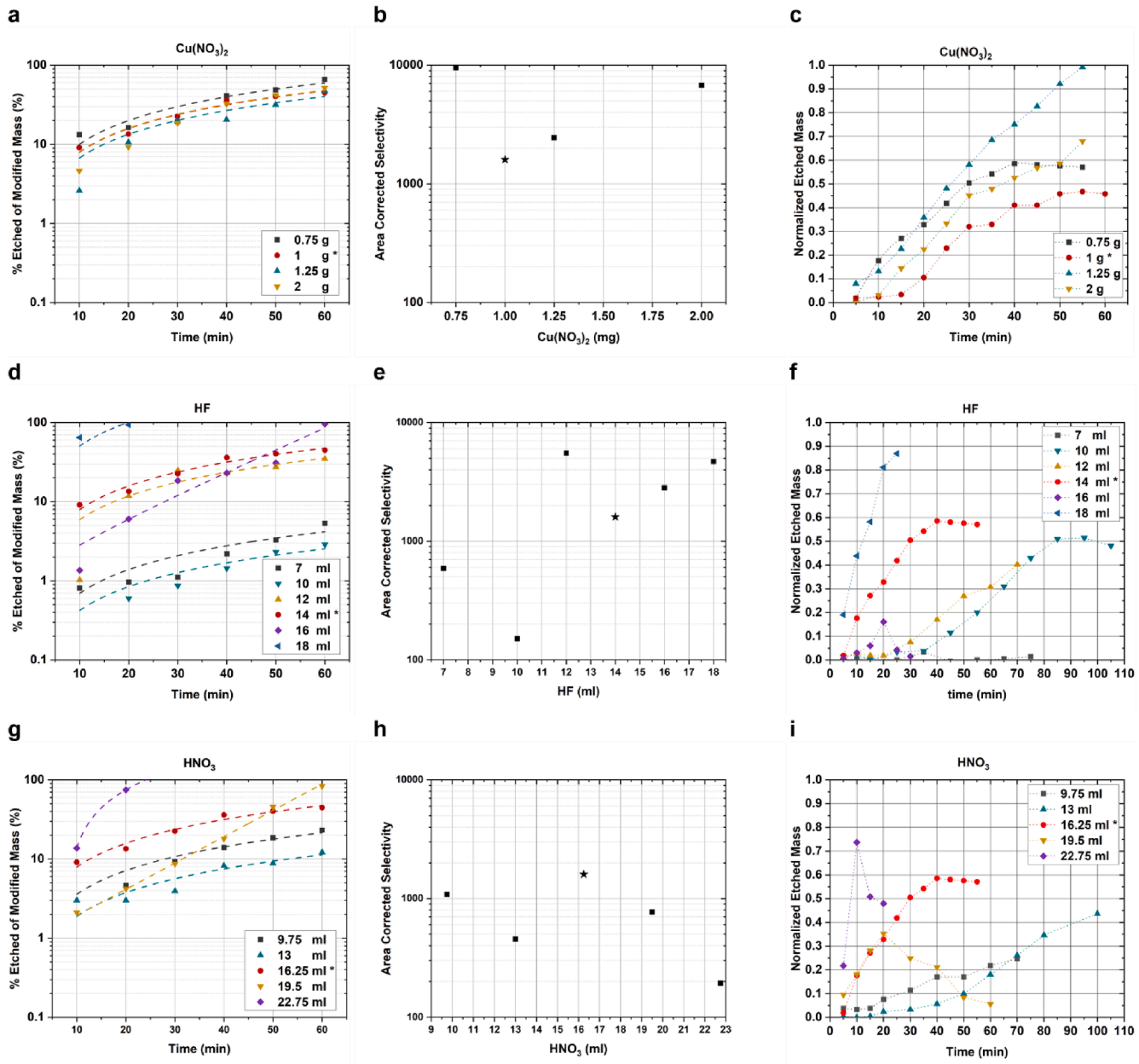

Fig. 7. (a), (d), (g) Etch rate of the laser-modified region over time for CALP. (b), (e), (h) Selectivity of the laser-modified region compared to unprocessed sample for CALP. (c), (f), (i) Normalized etched mass of the laser-modified region for SALP. The changing parameters are $Cu(NO_3)_2$ concentrations from 0.75 to 2 g (a), (b), (c); HF concentrations from 7 ml to 18 ml (d), (e), (f); HNO_3 concentrations from 9.75 to 22.75 ml in 100 ml of solution (g), (h), (i). The fixed parameters for each component variation are presented in Table 1. Our champion etchant concentration is marked by an asterisk (*).

(PW-91) approximation [72], and electron-nucleus interaction was modeled using ultrasoft pseudopotentials [73]. The plane-wave kinetic energy used to truncate the basis expansion was 40 Rydberg, and a vacuum distance of 14 Å was left between the images to reduce inter-image interaction. Atomic partial charges were calculated using the Bader charge decomposition as implemented by the Henkelman group [74].

According to the transmission electron microscopy (TEM) results from our previous study on a similar system [1] (presented in Supporting Information 5), the laser-modified regions appear to have a short-range order with a characteristic dimension of a few nanometers, interrupted by amorphous Si domains. The exact crystal structure of the ordered regions is not known; however, possible candidates are Si-I (FCC), Si-III (BCC), and Si-XII (Rhombohedral) phases, the latter two being known to form as a result of pressure or laser-induced damage [75]. However, our Raman results do not show any indication of Si-III or Si-XII but rather a diminished Si-I peak. It is fair then to assume that the difference in reactivity behavior of the laser-processed and unprocessed regions stems from the amorphous Si domains. Furthermore, although dissolution mechanisms of amorphous Si and silicon dioxide (SiO_2) have been shown to be rather complicated and dependent on a variety of parameters [76], overall amorphous Si surfaces are expected to show larger reactivity with respect to those that are crystalline, due to under-coordination, and abundance of defect sites [77]. In our DFT calculations, we therefore model the surfaces of the processed regions by amorphous SiO_2 while the unmodified Si is modeled by oxidized and unoxidized reconstructed Si ⟨1 0 0⟩ surfaces. In the damaged portions of the samples, oxidation is expected to take place very rapidly. Therefore, we do not consider the unoxidized amorphous Si.

The pristine Si ⟨1 0 0⟩ surface was modeled by a slab of five layers

with the two bottommost layers fixed to mimic bulk behavior. The Si ⟨100⟩ surface displayed several reconstructions to lower its surface energy, and a common reconstruction of this surface is the 2 × 1 or the dimer reconstruction [78], which was also applied in our calculations (Fig. 11 (a)). Next, an oxygen-decorated Si surface was built by placing rows of O atoms on the surface (Fig. 11 (b)). Finally, the amorphous SiO_2 simulation cell was constructed by extracting a 12 Å × 12 Å × 12 Å cube out of a previously conducted molecular dynamics (MD) investigation of a 3000-atom amorphous SiO_2 system [79]. In order to preserve stoichiometry, care was taken to include 36Si and 72O atoms. Once optimized in the bulk, a surface was formed via the extraction of the usual periodic slab geometry from the bulk, and a DFT-based geometry optimization was performed on this surface slab. The density was found to be 2.1 g/cm^3, close to the experimental value of 2.2 g/cm^3.

4. Results and discussion

To determine the effectiveness of each etching set, we have calculated the etch rate, etch pit radius distribution, and selectivity of laser-modified structures for CALP. In addition, the ratio of the area normalized etched mass of the surface over time is calculated for SALP. The etch rate is defined as the mass reduction of the laser-modified region versus the etching duration. The selectivity is defined as the etch rate of the laser-modified region divided by the etch rate of the unmodified region, indicating the rate at which the laser-modified region is etched away compared to the unmodified region. Note that it is also possible to use the sample volume instead of the mass since they only differ in a density factor which is almost the same for both the laser-modified region and unprocessed samples. The etch pit radius distribution analysis, which is an indication of the surface porosity and roughness, was performed for different concentrations of the solution components. The SEM images (Supporting Information 4) show that the etched surfaces of laser-modified samples contain distinctive features such as etch pits in all considered sets. The observed etch pits on the surface are formed due to the interaction of the different solutions with the c-Si segments. Our etchant solution is formulated to reveal the defects and thus the laser-modified regions. The etchant attacks and enlarges the defects, including dopant impurities on the surface of the Si rather than attacking the perfect (unprocessed) Si lattice. By utilizing chemical etching and etch pit analysis, it is possible to calculate the defect density (counting the etch pits and dividing them by the surface area) that is grown in the crystal lattice. However, it is a destructive characterization technique for determining the crystal quality of crystalline samples.

4.1. Correction factors calculation & etch pit radius distribution analysis

To calculate the etch rate and selectivity in terms of the reduced mass of the samples, the mass of laser-processed Si and the etched part must be determined. Thus, another unprocessed sample was used to find the mass change of the unmodified region. The mass difference between the laser-processed and the unprocessed samples is related to the laser-modified region. After each chemical process, the mass change of the unprocessed and processed samples was measured. The difference between the measured masses gives the etched mass of the laser-modified region, which needs to be corrected due to the complicated behavior of the etching process, coming from diffusion peculiarities of the mass and heat transports. Therefore, the mismatch of the initial masses before the chemical etching of unprocessed and laser-processed samples, the volume etched inside the laser-modified region, and the difference in the opening areas of the crystalline region and laser-modified region of the processed sample being subjected to etchant need to be modeled accordingly. To calculate laser-modified mass correctly in CALP structures, we hypothesize three correction factors, namely, the Correction Factor of Initial Mass (CFIM), Correction Factor of Etch Opening (CFEO), and Correction Factor of Attacked Area (CFAA).

To compare the SALP and CALP etching behaviors, the calculated mass reduction of the laser-processed region is normalized to the opening areas exposed to the etching solution (0.46 mm^2 and 4 mm^2 for CALP and SALP, respectively). Detailed information regarding the correction factors and calculations for both SALP and CALP structures is given in Supporting Information 6. The measured weight losses are utilized in the analyses and the etched volumes obtained from etched openings (SEM images in Supporting Information 4) and etched area cross-sections (IR camera image in Supporting Information 7).

The etch pit size distribution is determined using the built-in image processing toolbox of MATLAB [80] and the SEM images of subsurface-processed Si. It is worth mentioning that the subsurface and surface processing have an identical surface morphology. The histograms of etch pit size distribution for each material are presented in the Effects of Solution Components section. The SEM image of the champion etchant is shown in Fig. 6.

4.2. Effects of solution components on etchant chemistry

Etch rate and selectivity of the CALP structure, normalized etched mass and ratio of area normalized etched mass of the SALP structure, and etch pit radius distribution analysis for all chemical compositions were calculated based on the equations mentioned in Supporting Information 6. This information is categorized into three subgroups for each solution component. The etch rate for CALP and normalized etched mass for SALP structure are not constant across time since there is some latency before the etching starts. Thus, some delay may be required for the activation of Si-etchant reactions. Afterward, chemicals start to attack all regions until either the reactions saturate or the time frame ends. The etch rate is shown in Fig. 7 (a), (d), and (g) which is the percentage of cumulative etched mass over total laser-processed mass at each duration for CALP samples. The selectivity is shown in Fig. 7 (b), (e), and (h) which is the ratio of etch rates of the laser-modified and unprocessed regions after 60 min for CALP samples. The normalized etched mass over time shown in Fig. 7 (c), (f), and (i) which is cumulative etched mass of laser-processed region normalized to total laser-processed mass for SALP samples. Fig. 7 presents the variation of Cu$(NO_3)_2$ concentrations from 0.75 to 2 g, HF concentrations from 7 ml to 18 ml, and HNO_3 concentrations from 9.75 to 22.75 ml in 100 ml of solution. Further analysis on the effects of solution components on SALP and CALP is presented in Supporting Information 8.

4.2.1. Effects of copper nitrate – Cu(NO3)2 variation

The energy level of the Cu^{2+}/Cu system is higher than the valence band (VB) of Si [81]. For a given combination of HF/HNO_3, adding various amounts of Cu$(NO_3)_2$ corresponds to the Si surface being covered by copper nanoparticles (CuNPs) with different CuNPs surface coverage densities. These metal particles also catalyzed the etching of Si in HF/HNO_3 solution, and their presence resulted in the selective attacks of modified regions. The Cu^{2+} ions are reduced to solid Cu on the Si substrate and the oxidized surface is dissolved in HF. In addition, HNO_3 oxidizes the Si surface forming SiO_2 which is etched by the presence of HF.

In Fig. 7 (a), it can be seen that the etch rate of the laser-modified region decreases as the amount of Cu$(NO_3)_2$ increases from 0.75 to 1.25 g. However, the etch rate starts to increase for a higher amount of Cu$(NO_3)_2$ as it is seen at 2 g. In addition, as shown in Fig. 7 (b), the selectivity for CALP shows a different trend where it is highest for 0.75 g of Cu$(NO_3)_2$ and drops drastically then increases by increasing the Cu$(NO_3)_2$ amount. In Fig. 7 (c), the etched mass of the laser-modified region divided by the total etched mass is highest where the Cu$(NO_3)_2$ amount is 1 g. However, the etched mass decreases as the amount of Cu$(NO_3)_2$ further increases from 0.75 to 2 g.

The etch pit radius distribution, ranging between 1 – 15 μm, is shown in Fig. 8 (c). As the place of the laser modifications would not affect the surface properties, the etching solution results in similar surface

morphology. The etch pit size distribution is in the order of 1 μm. However, as the amount of $Cu(NO_3)_2$ increases, the resultant defects are found to have larger diameters.

4.2.2. Effects of hydrofluoric acid – HF variation

Increasing the amount of HF beyond a certain point for a given ratio of Cu and HNO_3 hinders the suspension of the CuNPs. Thus, CuNPs will be adsorbed on the surface at random locations and promote the etching process in their vicinity. This process is fast and creates more holes, leading to a spongy Si surface morphology.

As can be seen in Fig. 7 (d), a higher concentration of HF in the solution induces a very high etch rate and damages the sample, leading to poor surface morphology (Fig. S4 (e), (f)). The effect of higher HF is more pronounced in laser-modified regions than the unprocessed one, resulting in higher selectivity. In Fig. 7 (f), the etched mass of the laser-modified divided by the total etched mass region is well-behaved for 14 ml of HF, showing a reasonable etch rate. However, the modified region is harshly attacked in the etching solution with high HF concentration due to the nonlinear diffusion of the defects.

In Fig. 9 (c), the etch pit size distribution is below 15 μm when the HF concentration is moderate (7 ml to 14 ml). With a higher concentration of HF (above 16 ml), the etch pits exhibit larger defect sizes on the Si surfaces, as can be seen in the SEM image (Fig. S4 (e), (f)).

4.2.3. Effect of the oxidizing agent (nitric acid – HNO3) concentration

Cu ions are adsorbed on the Si surface. These ions attract minority negative charge carriers available in the p-type Si substrate. Thus, CuNPs collect electrons through the Cu/Si interface and transfer them to the solution. The conglomeration speed of CuNPs depends on the rate of metal ion removal. So, if the formation of the CuNPs is slower than its removal, there will be a high hole concentration on the surface that grows larger and larger. The amounts of oxidizing and reducing agents control how fast and aggressively Cu removes Si from the surface for a certain Cu amount. As a result, by fixing the amount of $Cu(NO_3)_2$ to 1 g, the combination of oxidation and reduction creates the intended structure. By tuning the oxidizing agent – HNO_3, it is possible to minimize the aggressiveness of the oxidation process in such a way that despite some distinct holes at the surface, the etchant does not wholly damage the Si surface and cause porosity. As discussed previously, increasing the HNO_3 controls the oxide formation on the CuNPs, which HF later etches. On the one hand, the presence of a high amount of HNO_3 in a given concentration of HF, i.e., 14 ml in 100 ml solution, causes CuNPs to become smaller. As a result, increasing HNO_3 makes the surface porous. On the other hand, the CuNPs must be maintained long enough to achieve the desired structure.

As shown in Fig. 7 (g), (h), etch rates increase while selectivity decreases by increasing the HNO_3 concentration in the CALP structure. This confirms that increasing the amount of oxidizing agent in the

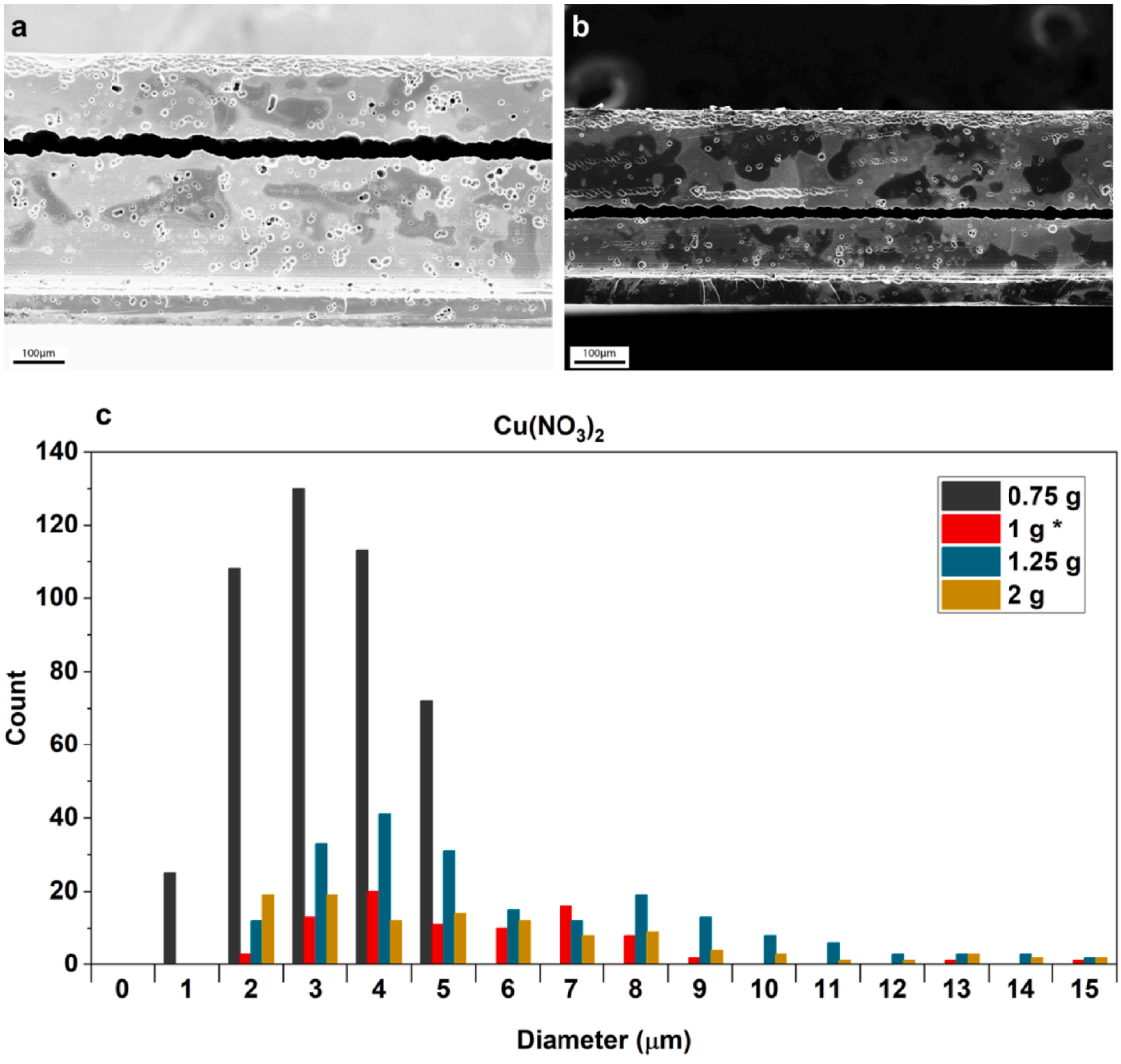

Fig. 8. SEM images of the surface of samples having $Cu(NO_3)_2$ concentrations of (a) 0.75 g and (b) 2 g in 100 ml of solution. (c) Etch pit radius distribution was obtained from SEM images by analyzing the surface morphology.

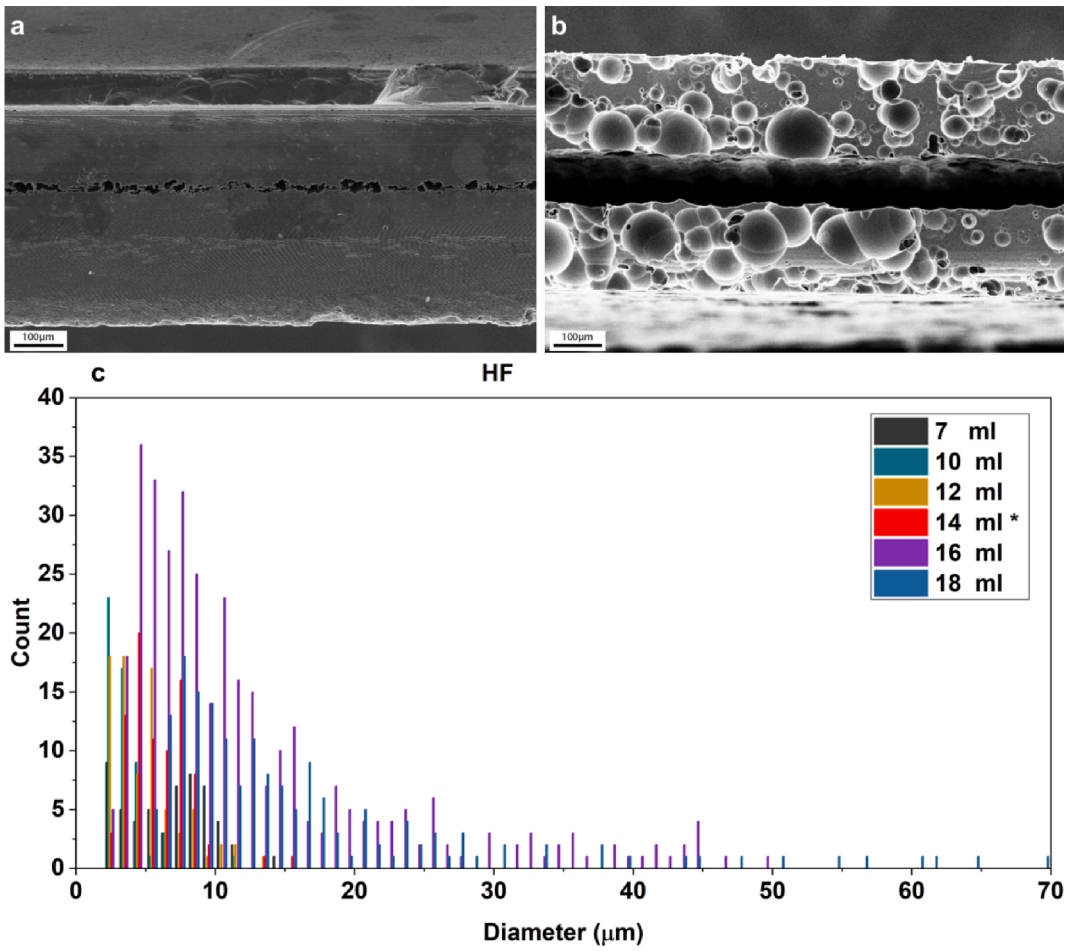

Fig. 9. SEM images of the surface of samples having HF concentrations of (a) 7 ml and (b) 18 ml in 100 ml of solution. (c) Etch pit radius distribution was obtained from SEM images by analyzing the surface morphology.

solution increases the etch rate of the laser-modified region more than the unprocessed sample. This behavior is due to the generation of more excess hole-type carriers at the surface, which accelerates the anodic chemical reactions. In Fig. 7 (i), the etched mass of the laser-modified sample divided by the total etched mass is increased and harshly attacked on both regions by the increasing amount of HNO_3 concentration as the etching time increases.

The quality of the etched surface is a function of HNO_3, i.e., increasing the amount of HNO_3 will result in the formation of an engraved surface. Fig. 10 (c) shows the etch pit radius size distribution is in the range of 1 – 70 μm except for the cases when HNO_3 concentration is high. The observed trends, particularly pertaining to the selectivity trends of the Cu and HF components, are corroborated with our DFT results presented in the next subsection.

The observed nonlinear etching behavior in all etching solutions can be attributed to the different ratios of amorphous and polycrystalline Si phases in laser-modified regions. These phases have different etching rates since amorphous is crystallographically disordered and polycrystalline is crystallographically locally ordered which is confirmed by TEM analysis (HRTEM, DAAF, SAED) presented in Supporting Information 5.

After surveying the above-mentioned chemical compositions, the optimal etchant having a reasonable etch rate, more than 1600 selectivity, and smooth and less defective unprocessed surface is determined. The optimal etchant concentration is found to be $HF:HNO_3:CH_3COOH:H_2O$ – 14.00:16.25:18.00:51.75 vol% with 0.01 g/ml $Cu(NO_3)_2{\cdot}3H_2O$, which we refer to as *the Champion Etchant*. The enhanced composition yields different chemical treatment durations required for specific applications. It is also dopant-type dependent and anisotropic (Supporting Information 9), which is beneficial for certain applications to etch laser-modified Si regions. The comparisons between MEMC and the enhanced composition in terms of orientation dependency and dopant type dependency are discussed in Supporting Information 9.

4.3. DFT results

Interaction of the surface with HF was modeled by means of simultaneously placing a single H and a single F on the surface, whereas the interaction with Cu was represented by a single Cu atom on the surface (See Fig. 11). Optimized geometries on the three surfaces can be seen in Fig. 11. The adsorption energies were calculated using the following equation:

$$E_{ads} = E_{tot} - E_{surf} - E_{mol} \quad (1)$$

where E_{tot} is the optimized energy of the entire system, E_{surf} is the energy of the surface (Si < 100>), oxygen-decorated Si < 100>, and amorphous SiO_2) without the H/F or Cu atoms, and E_{mol} is the energy of the adsorbates in isolation. In the case of the Cu adsorbate, E_{mol} corresponds to the total energy of a single Cu atom in a large simulation cell. In contrast, in the case of H and F, it represents the sum of the energies of a single H and a single F atom, calculated in isolation separately. Among the several geometries explored, a few of the most stable optimized geometries are shown in Fig. 11. The adsorption energies corresponding to the most stable geometries are shown in Table 2.

Several observations can be made based on these results. The amorphous SiO_2 surface appears to interact the weakest with the etchant

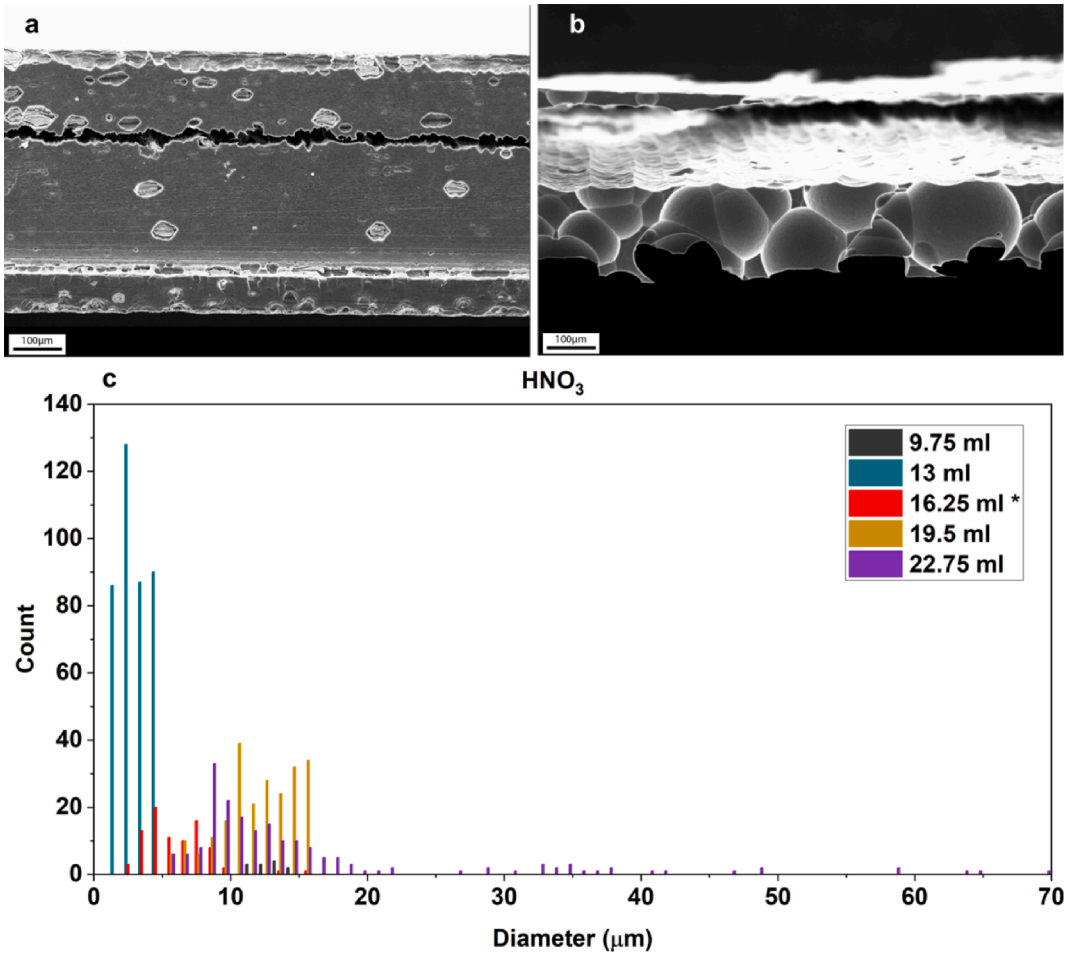

Fig. 10. SEM images of the surfaces of samples having HNO_3 concentrations of (a) 9.75 ml and (b) 22.75 ml in 100 ml of solution. (c) Etch pit radius distribution was obtained from SEM images by analyzing the surface morphology.

species among the surfaces studied. While there is no difference in H/F adsorption energies between the Si and the oxygen-decorated Si surfaces, Cu appears to interact significantly more strongly with the Si-O surface. On the oxygen-decorated Si surfaces, when the H/F ions are adsorbed on the oxygen atoms, their adsorption energy is considerably lower than partial adsorption on the Si atoms. On the other hand, Cu appears to benefit from the interaction with the oxygen atoms. In order to verify the ionic nature of the H and F atoms, the partial charges were calculated and found to be about −1.0 eV and + 1.0 eV for F and H adsorbates, respectively. The Bader charge of the Cu atom varies between 0 and + 0.3 eV depending on the adsorption site. This is consistent with the experimental insight that Cu clusters are first positively charged before reduction.

The HF component displays no selectivity between oxidized and pristine crystalline Si, as evidenced by the identical adsorption energies of the H and F ions. The adsorption energy of the HF unit on the c-Si surface is one order of magnitude larger than the amorphous surface. This significant difference between the adsorption energies explains the selectivity of the HF etchant towards the laser-processed surface. Etching of the surface proceeds through the desorption of adsorbed species. Therefore, the lower adsorption energy in the case of the amorphous oxide likely points towards facile desorption as well.

This trend continues with the catalyst component, namely the Cu atom. Cu adsorption on the oxidized c-Si surface is much larger than the a-SiO_2 considered. Since the Cu component should ideally desorb before it has time to form agglomerates, the significantly lower adsorption energy on the amorphous SiO_2 surface appears to be much more advantageous than the crystal surfaces. In particular, the Cu adsorption energy on the oxidized c-Si surface is particularly high, and the positive charge is larger. This behavior likely increases the dwelling time of Cu on the surface and encourages agglomeration, deactivating the catalyst.

We emphasize in passing one more time that the crystalline portions of the laser-processed domains appear to be a combination of nanocrystalline domains (Supporting Information 10) interrupted by grain boundaries with an amorphous phase. Therefore, the difference in dissolution behavior of the processed and unprocessed regions is dictated by these portions.

5. Conclusion

The optimization of a $Cu(NO_3)_2$-based etching solution on the novel selective etching of surface and subsurface laser-modified regions (CALP and SALP) is presented. The laser modifications are done by utilizing a nanosecond IR fiber laser on p-type c-Si wafers. The laser-modified samples are treated with a number of MEMC-like etchants in which the chemical component concentrations are varied in order to survey for an especially optimal etchant for laser-modified Si. To investigate the effect of each component, different sets of solutions are prepared by changing the concentrations. To obtain the etch rates, the mass difference of laser-modified and unprocessed samples is measured for up to 60 min. By applying correction factors of initial mass, etch opening, and attack area, the mass reduction of the laser-modified region and unprocessed c-Si samples are calculated. The selectivity of each set is calculated as the ratio of the laser-modified region and unprocessed c-Si samples. The c-Si smoothness is represented by calculating etch pit radius size distribution which was obtained from SEM images after 60

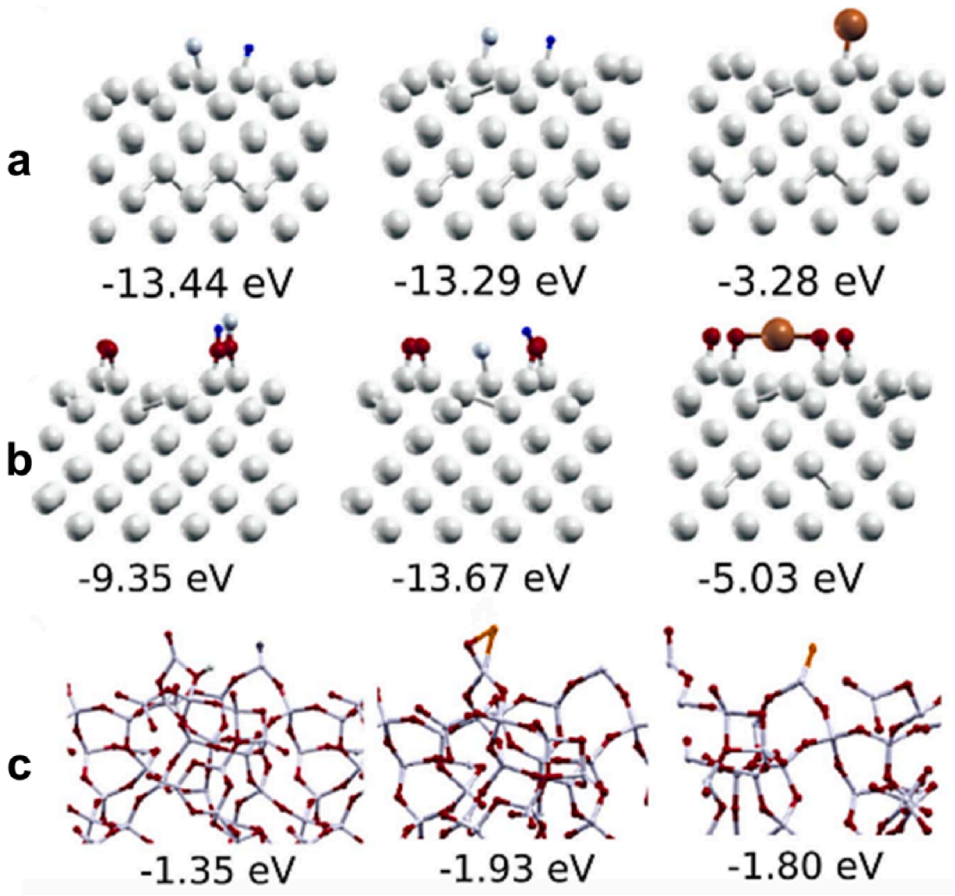

Fig. 11. Adsorption of HF and Cu on (a) reconstructed Si ⟨1 0 0⟩ surface; (b) oxygen-decorated Si ⟨1 0 0⟩ surface; (c) amorphous SiO2 surface. The Si, O, H, F, and Cu atoms are represented by white, red, gray, blue, and bronze spheres, respectively. The adsorption energies are given below each figure. (For interpretation of the references to colour in this figure legend, the reader is referred to the web version of this article.)

Table 2
Adsorption energies of the H + F complex and the Cu atom.

	H + F	Cu
Si < 100> 2x1 reconstruction	−13.44 eV	−3.28 eV
Si < 100> 2x1 reconstruction + O	−13.67 eV	−5.03 eV
Amorphous SiO_2 surface	−1.35 eV	−1.93 eV

min. The etch rate, selectivity, and surface morphology of subsurface laser-modified regions are well controlled during the experiments by varying the etching concentration of the etching solution components. The selection of the component concentrations depends on the desired applications since a different combination of etch rate, selectivity, and surface morphology can be achieved. For instance, decreasing $Cu(NO_3)_2$ to 0.75 g in 100 ml solution leads to fast and selective etching at the cost of c-Si surface smoothness. The etching rates show nonlinear behavior due to the presence of both amorphous and polycrystalline phases in the laser-modified regions confirmed by TEM. The adsorption energy calculations performed within the DFT method clearly corroborate the experimental findings. Calculated HF and Cu adsorption energies display significant diversity on the crystalline and amorphous surfaces. Since adsorption energy is a good indicator of reactivity, the difference in the adsorption energies can be interpreted as a potential explanation for the selectivity trends. In addition, decreasing HNO_3 leads to a low etch rate and selectivity while providing smooth c-Si surface morphology. Some applications which may use small samples require high selectivity but a low etch rate which can be achieved by increasing the $Cu(NO_3)_2$ to 2 g in 100 ml solution. After an extensive survey of component concentrations, we achieved an optimum composition of HF: HNO_3:CH_3COOH:H_2O – 14.00:16.25:18.00:51.75 vol% with 0.01 g/ml $Cu(NO_3)_2{\cdot}3H_2O$ as *the champion etchant* for surface and subsurface laser-modified Si which shows more than 1600 selectivity as well as etch pit sizes in the range of 1 – 10 μm indicating relatively smooth and low defective surface. In addition, by comparing SALP and CALP results, it is concluded that surface etching has a higher etch rate which is expectable due to heat transfer and diffusion restrictions in the subsurface samples. In order to demonstrate the capability of this especially optimized etchant, a micro-pillar array is fabricated with a controlled size/depth combination in a two-step process. With this technique, micro-pillars with lateral dimensions as small as 9 μm × 9 μm and with a depth as large as 118 μm were successfully fabricated yielding an aspect ratio > 13. We successfully utilized our novel technique to fabricate periodic arrays of pillars with a controlled aspect ratio as a light-trapping structure for use in photonic devices such as photon detectors and solar cells. Direct writing of 3D Si structures is expected to attract increasing attention in advanced device fabrication technologies including, but not limited to MEMS.

CRediT authorship contribution statement

Mona Zolfaghari Borra: Data curation, Formal analysis, Investigation, Validation, Visualization, Writing – original draft. **Behrad Radfar:** Data curation, Formal analysis, Investigation, Software, Visualization, Writing – original draft. **Hisham Nasser:** Data curation, Formal analysis, Investigation, Methodology, Supervision, Writing – review & editing. **Tahir Çolakoğlu:** Investigation, Methodology, Supervision, Writing – review & editing. **Onur Tokel:** Conceptualization, Investigation, Methodology, Supervision, Writing – review & editing. **Ahmet**

Turnalı: Methodology. **Merve Demirtaş:** Investigation, Software, Formal analysis. **Dilek Işık Taşgın:** Investigation, Methodology. **Hande Üstünel:** Data curation, Formal analysis, Investigation, Methodology, Software, Visualization, Writing – original draft. **Daniele Toffoli:** Software, Writing – original draft, Data curation, Formal analysis, Investigation. **Fatih Ömer İlday:** Funding acquisition, Resources, Supervision, Writing – review & editing. **Raşit Turan:** Funding acquisition, Resources, Supervision, Writing – review & editing. **Ihor Pavlov:** Conceptualization, Formal analysis, Investigation, Methodology, Resources, Software, Supervision, Validation, Writing – review & editing. **Alpan Bek:** Conceptualization, Funding acquisition, Methodology, Project administration, Resources, Software, Supervision, Visualization, Writing – review & editing.

Declaration of competing interest

The authors declare that they have no known competing financial interests or personal relationships that could have appeared to influence the work reported in this paper.

Data availability

Data will be made available on request.

Acknowledgments

M.Z.B. and B.R. contributed equally to this work. This work was supported by the Scientific and Technological Research Council of Turkey (TÜBİTAK) under grant nr. 113M931 (I.P.), 118E995 (A.B.) and 20AG002 (R.T.); the European Research Council (ERC) through the NLL (grant nr. 617521), and the SUPERSONIC (grant nr. 966846) projects (F.Ö.İ.); the Turkish Academy of Sciences Young Investigator Program (TUBA-GEBIP) Award (O.T.). B.R. acknowledges the financial support of the Academy of Finland (grant nr. 331313). We kindly thank Dr. Mehmet Koç of ODTÜ-GÜNAM for help with some of the figures.

Appendix A. Supplementary data

Supplementary data to this article can be found online at https://doi.org/10.1016/j.optlastec.2024.111022.

References

[1] O. Tokel, et al., In-chip microstructures and photonic devices fabricated by nonlinear laser lithography deep inside silicon, Nat. Photonics 11 (10) (Oct. 2017) 639–645, https://doi.org/10.1038/s41566-017-0004-4.
[2] I. Pavlov, E. Dülgergil, E. Ilbey, and F. Ö. Ilday, 10 W, 10 ns, 50 kHz all-fiber laser at 1.55 μm, in Conference on Lasers and Electro-Optics 2012, Washington, D.C.: OSA, 2012, p. CTu2M.5. doi: 10.1364/CLEO_SI.2012.CTu2M.5.
[3] A.H. Nejadmalayeri, P.R. Herman, J. Burghoff, M. Will, S. Nolte, A. Tünnermann, Inscription of optical waveguides in crystalline silicon by mid-infrared femtosecond laser pulses, Opt. Lett. 30 (9) (May 2005) 964, https://doi.org/10.1364/OL.30.000964.
[4] B. Öktem, et al., Nonlinear laser lithography for indefinitely large-area nanostructuring with femtosecond pulses, Nat. Photonics 7 (11) (Nov. 2013) 897–901, https://doi.org/10.1038/nphoton.2013.272.
[5] M. Chambonneau, D. Grojo, O. Tokel, F.Ö. Ilday, S. Tzortzakis, S. Nolte, In-volume laser direct writing of silicon—challenges and opportunities, Laser Photon Rev. 15 (11) (2021) Nov, https://doi.org/10.1002/lpor.202100140.
[6] L. Jiang, A.-D. Wang, B. Li, T.-H. Cui, Y.-F. Lu, Electrons dynamics control by shaping femtosecond laser pulses in micro/nanofabrication: modeling, method, measurement and application, Light Sci. Appl. 7 (2) (Aug. 2017) 17134, https://doi.org/10.1038/lsa.2017.134.
[7] H. Tang, et al., Experimental quantum fast hitting on hexagonal graphs, Nat. Photonics 12 (12) (Dec. 2018) 754–758, https://doi.org/10.1038/s41566-018-0282-5.
[8] H. Tang, et al., "Experimental two-dimensional quantum walk on a photonic chip," Sci. Adv., vol. 4, no. 5, May 2018, doi: 10.1126/sciadv.aat3174.
[9] K. Kumar, K.K. Lee, J. Li, J. Nogami, N.P. Kherani, P.R. Herman, Quantized structuring of transparent films with femtosecond laser interference, Light Sci. Appl. 3 (3) (Mar. 2014) e157–e, https://doi.org/10.1038/lsa.2014.38.
[10] R. Osellame, H.J.W.M. Hoekstra, G. Cerullo, M. Pollnau, Femtosecond laser microstructuring: an enabling tool for optofluidic lab-on-chips, Laser Photon Rev 5 (3) (May 2011) 442–463, https://doi.org/10.1002/lpor.201000031.
[11] R.G.H. van Uden, et al., Ultra-high-density spatial division multiplexing with a few-mode multicore fibre, Nat. Photonics 8 (11) (Nov. 2014) 865–870, https://doi.org/10.1038/nphoton.2014.243.
[12] C. Hnatovsky, R.S. Taylor, E. Simova, V.R. Bhardwaj, D.M. Rayner, P.B. Corkum, Polarization-selective etching in femtosecond laser-assisted microfluidic channel fabrication in fused silica, Opt. Lett. 30 (14) (Jul. 2005) 1867, https://doi.org/10.1364/OL.30.001867.
[13] K. Sugioka, et al., Femtosecond laser 3D micromachining: a powerful tool for the fabrication of microfluidic, optofluidic, and electrofluidic devices based on glass, Lab Chip 14 (18) (2014) 3447–3458, https://doi.org/10.1039/C4LC00548A.
[14] M.S. Giridhar, K. Seong, A. Schülzgen, P. Khulbe, N. Peyghambarian, M. Mansuripur, Femtosecond pulsed laser micromachining of glass substrates with application to microfluidic devices, Appl. Opt. 43 (23) (Aug. 2004) 4584, https://doi.org/10.1364/AO.43.004584.
[15] M. Z. Borra, et al., "Slicing Crystalline Silicon Wafer by Deep Subsurface Laser Processing and Selective Chemical Etching," in 2019 Conference on Lasers and Electro-Optics Europe & European Quantum Electronics Conference (CLEO/Europe-EQEC), IEEE, Jun. 2019, pp. 1–1. doi: 10.1109/CLEOE-EQEC.2019.8872359.
[16] M. Borra Zolfaghari, "Implementation of strong light-matter interaction for fabrication and light management of thin crystal silicon solar cells," Middle East Technical University, 2021. Accessed: Feb. 11, 2024. [Online]. Available: https://hdl.handle.net/11511/91687.
[17] E. Granados, M. Martinez-Calderon, M. Gomez, A. Rodriguez, S.M. Olaizola, Photonic structures in diamond based on femtosecond UV laser induced periodic surface structuring (LIPSS), Opt. Express 25 (13) (Jun. 2017) 15330, https://doi.org/10.1364/OE.25.015330.
[18] J. Bonse, et al., "Applications of laser-induced periodic surface structures (LIPSS)," U. Klotzbach, K. Washio, and R. Kling, Eds., Feb. 2017, p. 100920N. doi: 10.1117/12.2250919.
[19] S. Dottermusch, et al., Micro-cone textures for improved light in-coupling and retroreflection-inspired light trapping at the front surface of solar modules, Prog. Photovolt. Res. Appl. 27 (7) (Jul. 2019) 593–602, https://doi.org/10.1002/pip.3133.
[20] B. Radfar, F. Es, R. Turan, Effects of different laser modified surface morphologies and post-texturing cleanings on c-Si solar cell performance, Renew. Energy 145 (Jan. 2020) 2707–2714, https://doi.org/10.1016/j.renene.2019.08.031.
[21] J. Ding, et al., A laser texturing study on multi-crystalline silicon solar cells, Sol. Energy Mater. Sol. Cells 214 (Aug. 2020) 110587, https://doi.org/10.1016/j.solmat.2020.110587.
[22] S. Kontermann, T. Gimpel, A.L. Baumann, K.-M. Guenther, W. Schade, Laser processed black silicon for photovoltaic applications, Energy Procedia 27 (2012) 390–395, https://doi.org/10.1016/j.egypro.2012.07.082.
[23] M. Otto, et al., Black silicon photovoltaics, Adv. Opt. Mater. 3 (2) (Feb. 2015) 147–164, https://doi.org/10.1002/adom.201400395.
[24] X. Liu, B. Radfar, K. Chen, T. P. Pasanen, V. Vähänissi, and H. Savin, "Tailoring Femtosecond-Laser Processed Black Silicon for Reduced Carrier Recombination Combined with >95% Above-Bandgap Absorption," *Adv Photonics Res*, vol. 3, no. 4, Apr. 2022, doi: 10.1002/adpr.202100234.
[25] V.Y. Fedorov, M. Chanal, D. Grojo, S. Tzortzakis, Accessing extreme spatiotemporal localization of high-power laser radiation through transformation optics and scalar wave equations, Phys. Rev. Lett. 117 (4) (Jul. 2016) 043902, https://doi.org/10.1103/PhysRevLett.117.043902.
[26] M. Chambonneau, Q. Li, M. Chanal, N. Sanner, D. Grojo, Writing waveguides inside monolithic crystalline silicon with nanosecond laser pulses, Opt. Lett. 41 (21) (Nov. 2016) 4875, https://doi.org/10.1364/OL.41.004875.
[27] M. Chanal, V.Y. Fedorov, M. Chambonneau, R. Clady, S. Tzortzakis, D. Grojo, Crossing the threshold of ultrafast laser writing in bulk silicon, Nat. Commun. 8 (1) (Oct. 2017) 773, https://doi.org/10.1038/s41467-017-00907-8.
[28] G.C. Giakos, et al., "Laser imaging through scattering media," in Proceedings of the 21st IEEE Instrumentation and Measurement Technology Conference (IEEE Cat. No.04CH37510), IEEE, pp. 433–437. doi: 10.1109/IMTC.2004.1351081.
[29] K.M. Davis, K. Miura, N. Sugimoto, K. Hirao, Writing waveguides in glass with a femtosecond laser, Opt. Lett. 21 (21) (Nov. 1996) 1729, https://doi.org/10.1364/OL.21.001729.
[30] S. Jesse, A.J. Pedraza, J.D. Fowlkes, J.D. Budai, Etching-enhanced ablation and the formation of a microstructure in silicon by laser irradiation in an SF_6 atmosphere, J. Mater. Res. 17 (5) (May 2002) 1002–1013, https://doi.org/10.1557/JMR.2002.0148.
[31] T.-H. Her, R.J. Finlay, C. Wu, S. Deliwala, E. Mazur, Microstructuring of silicon with femtosecond laser pulses, Appl. Phys. Lett. 73 (12) (Sep. 1998) 1673–1675, https://doi.org/10.1063/1.122241.
[32] D. Riedel, J.L. Hernandez-Pozos, R.E. Palmer, K.W. Kolasinski, Fabrication of ordered arrays of silicon cones by optical diffraction in ultrafast laser etching with SF6, Appl. Phys. A 78 (3) (Feb. 2004) 381–385, https://doi.org/10.1007/s00339-002-1938-y.
[33] D. Mills, K.W. Kolasinski, Laser-etched silicon pillars and their porosification, J. Vac. Sci. Technol. A 22 (4) (Jul. 2004) 1647–1651, https://doi.org/10.1116/1.1690253.
[34] D. Mills, K.W. Kolasinski, Non-lithographic method of forming ordered arrays of silicon pillars and macropores, J. Phys. D Appl. Phys. 38 (4) (Feb. 2005) 632–636, https://doi.org/10.1088/0022-3727/38/4/017.

[35] R. A. Sabet, A. Ishraq, and O. Tokel, "Laser nanofabrication deep inside silicon wafers," in 2021 Conference on Lasers and Electro-Optics Europe and European Quantum Electronics Conference, OSA Technical Digest (Optica Publishing Group, 2021), 2021, p. paper cm_2_6. Accessed: Feb. 11, 2024. [Online]. Available: https://opg.optica.org/abstract.cfm?URI=CLEO_Europe-2021-cm_2_6.
[36] R. Asgari Sabet, A. Saltık, and O. Tokel, "Creating efficient nano-gratings buried in silicon through laser nano-lithography," in Laser Applications in Microelectronic and Optoelectronic Manufacturing (LAMOM) XXVIII, L. Gemini, A. Narazaki, and J. Kleinert, Eds., SPIE, Mar. 2023, p. 32. doi: 10.1117/12.2649043.
[37] S.W. Bedell, D.K. Sadana, K. Fogel, H. Chen, A. Domenicucci, Quick turnaround technique for highlighting defects in thin Si/SiGe bilayers, Electrochem. Solid St. 7 (5) (2004) G105, https://doi.org/10.1149/1.1676116.
[38] B. Miao, et al., Improved metal assisted chemical etching method for uniform, vertical and deep silicon structure, J. Micromech. Microeng. 27 (5) (May 2017) 055019, https://doi.org/10.1088/1361-6439/aa6872.
[39] L. Romano, et al., Metal assisted chemical etching of silicon in the gas phase: a nanofabrication platform for X-ray optics, Nanoscale Horiz. 5 (5) (2020) 869–879, https://doi.org/10.1039/C9NH00709A.
[40] N. Van Toan, M. Toda, T. Hokama, T. Ono, Cantilever with high aspect ratio nanopillars on its top surface for moisture detection in electronic products, Adv. Eng. Mater. 19 (11) (Nov. 2017), https://doi.org/10.1002/adem.201700203.
[41] M.Z. Mohd Zin, E.H. Felix, Y. Wahab, M.N. Bakar, Process development and characterization towards microstructural realization using laser micromachining for MEMS, SN Appl Sci 2 (5) (May 2020) 912, https://doi.org/10.1007/s42452-020-2715-2.
[42] R. Dumke, M. Volk, T. Müther, F.B.J. Buchkremer, G. Birkl, W. Ertmer, Micro-optical realization of arrays of selectively addressable dipole traps: a scalable configuration for quantum computation with atomic qubits, Phys. Rev. Lett. 89 (9) (Aug. 2002) 097903, https://doi.org/10.1103/PhysRevLett.89.097903.
[43] R. Soref, Mid-infrared photonics in silicon and germanium, Nat. Photonics 4 (8) (Aug. 2010) 495–497, https://doi.org/10.1038/nphoton.2010.171.
[44] Z. Fang, Q.Y. Chen, C.Z. Zhao, A review of recent progress in lasers on silicon, Opt. Laser Technol. 46 (Mar. 2013) 103–110, https://doi.org/10.1016/j.optlastec.2012.05.041.
[45] X. Li, et al., Improvement of saw damage removal to fabricate uniform black silicon nanostructure on large-area multi-crystalline silicon wafers, Sol. Energy 204 (Jul. 2020) 577–584, https://doi.org/10.1016/j.solener.2020.03.072.
[46] X. Wei, Z. Xiao, Z. Yue, H. Huang, L. Zhou, Texturization of diamond wire sawn multi-crystalline silicon wafers by micro-droplet etching, Mater. Sci. Semicond. Process. 115 (Aug. 2020) 105075, https://doi.org/10.1016/j.mssp.2020.105075.
[47] M. Zolfaghari Borra, et al., A feasibility study for controlling self-organized production of plasmonic enhancement interfaces for solar cells, Appl. Surf. Sci. 318 (Nov. 2014) 43–50, https://doi.org/10.1016/j.apsusc.2013.12.088.
[48] T.E. Scheul, E. Khorani, T. Rahman, M.D.B. Charlton, S.A. Boden, Wavelength and angle resolved reflectance measurements of pyramidal textures for crystalline silicon photovoltaics, Prog. Photovolt. Res. Appl. 28 (12) (Dec. 2020) 1248–1257, https://doi.org/10.1002/pip.3319.
[49] H. Nasser, M.Z. Borra, E.H. Çiftpınar, B. Eldeeb, R. Turan, Fourteen percent efficiency ultrathin silicon solar cells with improved infrared light management enabled by hole-selective transition metal oxide full-area rear passivating contacts, Prog. Photovolt. Res. Appl. 30 (8) (Aug. 2022) 823–834, https://doi.org/10.1002/pip.3510.
[50] F. Es, G. Baytemir, M. Kulakci, R. Turan, Metal-assisted nano-textured solar cells with SiO2/Si3N4 passivation, Sol. Energy Mater. Sol. Cells 160 (Feb. 2017) 269–274, https://doi.org/10.1016/j.solmat.2016.10.032.
[51] T.H. Fung, et al., Improved emitter performance of RIE black silicon through the application of in-situ oxidation during POCl3 diffusion, Sol. Energy Mater. Sol. Cells 210 (Jun. 2020) 110480, https://doi.org/10.1016/j.solmat.2020.110480.
[52] B. Schwartz, H. Robbins, Chemical Etching of Silicon: IV. Etching Technology, J. Electrochem. Soc. 123 (12) (Dec. 1976) 1903–1909, https://doi.org/10.1149/1.2132721.
[53] W.C. Dash, Copper precipitation on dislocations in silicon, J. Appl. Phys. 27 (10) (Oct. 1956) 1193–1195, https://doi.org/10.1063/1.1722229.
[54] E. Sirtl, A. Adler, Chromsäure-Flußsäure als spezifisches System zur Ätzgrubenentwicklung auf Silizium, Int. J. Mater. Res. 52 (8) (Aug. 1961) 529–531, https://doi.org/10.1515/ijmr-1961-520806.
[55] H. Seiter, "INTEGRATIONAL ETCHING METHODS," in *Semiconductor Silicon 1977: Proceedings of the Third International Symposium on Silicon Materials Science and Technology*, H. R. Huff and E. Sirtl, Eds., Philadelphia: Cornell University, May 1977, pp. 187–196. Accessed: Feb. 11, 2024. [Online]. Available: https://books.google.com/books?id=A8RQAAAAYAAJ&pg=PA187.
[56] T.C. Chandler, MEMC etch—a chromium trioxide-free etchant for delineating dislocations and slip in silicon, J. Electrochem. Soc. 137 (3) (Mar. 1990) 944–948, https://doi.org/10.1149/1.2086584.
[57] Y. Saito, Y. Matsushita, Etching solution for evaluating crystal faults, Accessed: Feb. 11, 2024. [Online]. Available: EP0281115 B1, Mar. 02 (1988) https://patents.google.com/patent/EP0281115B1.
[58] DHHS (NIOSH), "NIOSH technical report: control technology assessment: metal plating and cleaning operations," Dec. 1984. doi: 10.26616/NIOSHPUB85102.
[59] DHHS (NIOSH), "Criteria for a recommended standard: occupational exposure to hexavalent chromium," Jan. 2013. doi: 10.26616/NIOSHPUB2013128.
[60] R. Elbersen, W. Vijselaar, R.M. Tiggelaar, H. Gardeniers, J. Huskens, Fabrication and doping methods for silicon nano- and micropillar arrays for solar-cell applications: a review, Adv. Mater. 27 (43) (Nov. 2015) 6781–6796, https://doi.org/10.1002/adma.201502632.
[61] E. Garnett, P. Yang, Light trapping in silicon nanowire solar cells, Nano Lett. 10 (3) (Mar. 2010) 1082–1087, https://doi.org/10.1021/nl100161z.
[62] Y. Wang, et al., Maskless inverted pyramid texturization of silicon, Sci. Rep. 5 (1) (Jun. 2015) 10843, https://doi.org/10.1038/srep10843.
[63] S. Greco, S. Dal Zilio, A. Bek, M. Lazzarino, D. Naumenko, Frequency modulated raman spectroscopy, ACS Photonics 5 (2) (Feb. 2018) 312–317, https://doi.org/10.1021/acsphotonics.7b01026.
[64] D. Naumenko, V. Toffoli, S. Greco, S. Dal Zilio, A. Bek, M. Lazzarino, A micromechanical switchable hot spot for SERS applications, Appl. Phys. Lett. 109 (13) (2016) Sep, https://doi.org/10.1063/1.4964123.
[65] W. Kern, The evolution of silicon wafer cleaning technology, J. Electrochem. Soc. 137 (6) (Jun. 1990) 1887–1892, https://doi.org/10.1149/1.2086825.
[66] K.Q. Peng, et al., Fabrication of single-crystalline silicon nanowires by scratching a silicon surface with catalytic metal particles, Adv. Funct. Mater. 16 (3) (Feb. 2006) 387–394, https://doi.org/10.1002/adfm.200500392.
[67] Z.P. Huang, N. Geyer, L.F. Liu, M.Y. Li, P. Zhong, Metal-assisted electrochemical etching of silicon, Nanotechnology 21 (46) (Nov. 2010) 465301, https://doi.org/10.1088/0957-4484/21/46/465301.
[68] Y.-T. Lu, A.R. Barron, Anti-reflection layers fabricated by a one-step copper-assisted chemical etching with inverted pyramidal structures intermediate between texturing and nanopore-type black silicon, J. Mater. Chem. A Mater. 2 (30) (Jun. 2014) 12043, https://doi.org/10.1039/C4TA02006E.
[69] X. Leng, C. Wang, Z. Yuan, Progress in metal-assisted chemical etching of silicon nanostructures, Procedia CIRP 89 (2020) 26–32, https://doi.org/10.1016/j.procir.2020.05.114.
[70] L. Yang, et al., The fabrication of micro/nano structures by laser machining, Nanomaterials 9 (12) (Dec. 2019) 1789, https://doi.org/10.3390/nano9121789.
[71] P. Giannozzi, et al., QUANTUM ESPRESSO: a modular and open-source software project for quantum simulations of materials, J. Phys. Condens. Matter 21 (39) (Sep. 2009) 395502, https://doi.org/10.1088/0953-8984/21/39/395502.
[72] J. P. Perdew, "Unified theory of exchange and correlation beyond the local density approximation," in *Electronic Structure of Solids '91: Proceedings of the 75. WE-Heraeus-Seminar and 21st Annual International Symposium on Electronic Structure of Solids*, P. Ziesche and H. Eschrig, Eds., Akademie Verlag, 1991, pp. 11–20.
[73] D. Vanderbilt, Soft self-consistent pseudopotentials in a generalized eigenvalue formalism, Phys. Rev. B 41 (11) (Apr. 1990) 7892–7895, https://doi.org/10.1103/PhysRevB.41.7892.
[74] W. Tang, E. Sanville, G. Henkelman, A grid-based Bader analysis algorithm without lattice bias, J. Phys. Condens. Matter 21 (8) (Feb. 2009) 084204, https://doi.org/10.1088/0953-8984/21/8/084204.
[75] N. Fujisawa, J.S. Williams, M.V. Swain, On the cyclic indentation behavior of crystalline silicon with a sharp tip, J. Mater. Res. 22 (11) (Nov. 2007) 2992–2997, https://doi.org/10.1557/JMR.2007.0406.
[76] X. Chen, C. Liu, J. Ke, J. Zhang, X. Shu, J. Xu, Subsurface damage and phase transformation in laser-assisted nanometric cutting of single crystal silicon, Mater. Des. 190 (May 2020) 108524, https://doi.org/10.1016/j.matdes.2020.108524.
[77] P.M. Dove, N. Han, A.F. Wallace, J.J. De Yoreo, Kinetics of amorphous silica dissolution and the paradox of the silica polymorphs, Proc. Natl. Acad. Sci. 105 (29) (Jul. 2008) 9903–9908, https://doi.org/10.1073/pnas.0803798105.
[78] C. Yang, H.C. Kang, Geometry of dimer reconstruction on the C(100), Si(100), and Ge(100) surfaces, J. Chem. Phys. 110 (22) (Jun. 1999) 11029–11037, https://doi.org/10.1063/1.479039.
[79] S. Le Roux, V. Petkov, ISAACS – interactive structure analysis of amorphous and crystalline systems, J. Appl. Cryst. 43 (1) (Feb. 2010) 181–185, https://doi.org/10.1107/S0021889809051929.
[80] The MathWorks Inc., "MATLAB." The MathWorks Inc., 2024. Accessed: Feb. 11, 2024. [Online]. Available: https://www.mathworks.com.
[81] Y. Wang, Y. Liu, L. Yang, W. Chen, X. Du, A. Kuznetsov, Micro-structured inverted pyramid texturization of Si inspired by self-assembled Cu nanoparticles, Nanoscale 9 (2) (2017) 907–914, https://doi.org/10.1039/C6NR08126F.